Front. Phys. 10(5), 104101 (2015)
DOI 10.1007/s11467-015-0508-7

RESEARCH ARTICLE

Design of a sector bowtie nano-rectenna for optical power and infrared detection

Kai Wang[1,2], Haifeng Hu[1], Shan Lu[1], Lingju Guo[1,*], Tao He[1,†]

[1] *CAS Key Laboratory of Nanosystem and Hierarchical Fabrication, National Center for Nanoscience and Technology, Beijing 100190, China*

[2] *University of Chinese Academy of Sciences, Beijing 100049, China*

*Corresponding authors. E-mail: *guolj@nanoctr.cn, †het@nanoctr.cn*

Received August 1, 2015; accepted September 10, 2015

We designed a sector bowtie nanoantenna integrated with a rectifier (Au–TiO_x–Ti diode) for collecting infrared energy. The optical performance of the metallic bowtie nanoantenna was numerically investigated at infrared frequencies (5–30 μm) using three-dimensional frequency-domain electromagnetic field calculation software based on the finite element method. The simulation results indicate that the resonance wavelength and local field enhancement are greatly affected by the shape and size of the bowtie nanoantenna, as well as the relative permittivity and conductivity of the dielectric layer. The output current of the rectified nano-rectenna is substantially at nanoampere magnitude with an electric field intensity of 1 V/m. Moreover, the power conversion efficiency for devices with three different substrates illustrates that a substrate with a larger refractive index yields a higher efficiency and longer infrared response wavelength. Consequently, the optimized structure can provide theoretical support for the design of novel optical rectennas and fabrication of optoelectronic devices.

Keywords nano-rectenna, MIM diode, surface plasmon resonance, local field enhancement, photoelectric conversion efficiency

PACS numbers 41.20.Jb, 52.40.Fd, 81.05.Bx, 84.60.Jt

1 Introduction

The nano-rectenna consisting of a receiving optical nanoantenna and metal–insulator–metal (MIM) rectifier has attracted great attention over past decades because of its broad applications in high-efficiency solar cells [1], infrared detectors [2], biochemical sensors [3], quantum single-photon sources [4], and electronic device cooling [5]. The metallic nanoantenna based on surface plasmon resonance [6–10] and restricted to the subwavelength scale [11, 12] can effectively collect optical energy in the visible and infrared frequency ranges. The resulting MIM rectifier can convert AC oscillation to DC power. Many efforts have been made recently to obtain maximum field enhancement and higher rectifier conversion efficiency by designing the nanoantenna and MIM diode both experimentally and theoretically. Popular rectenna designs [13] have a thin-film Ni–NiO–Ni diode with an integrated infrared antenna and exhibit the smallest contact area (110 nm × 110 nm) ever reported for thin-film MIM diodes so as to obtain a fast optical response. The DC signal generated in the diode is measured by detection of CO_2 laser radiation with a wavelength of 10.6 μm. Various antenna structures (such as dipole [14], bowtie [15], and spiral [16] rectennas) have been fabricated to investigate the coupling of the incident light. Various types of MIM diodes, for example, Ni–NiO–Cr (1 μm^2) [17], Ni–NiO–Ni (0.018 μm^2) [18], Al–AlO_x–Pt (0.0056 μm^2) [14], Ni–NiO–Cu (0.008 μm^2) [19], and Cu–CuO–Au (0.0045 μm^2) [20], have been reported. Some improvements have been achieved by increasing the work function difference between the two metal electrodes to obtain highly nonlinear $I(V)$ behavior and/or by reducing the contact area of the tunneling junction to obtain impedance matching between the antenna and diode. However, most of the experimental investigations to date have characterized the electrical performance of the rectenna, and the optical response of the devices has seldom been studied, possibly because there is no mature theory or numerical analysis of the nano-rectenna. Theoretical studies of the antenna alone and the MIM diode alone have been rel-

atively thorough, but very few theoretical studies have been reported for the entire rectenna consisting of both the antenna and the tunneling diode. Local field enhancement in the feed gap of the antenna is due to surface plasmon resonance coupled by two metallic strips [21]. A near-field intensity enhancement $|E|^2$ exceeding 10^3 has been obtained at the center of the antenna gap [22, 23]. If the feed gap of a dipole or bowtie antenna can be filled with metals to attain perfect load matching, the induced current could be on the order of 10^{-15} A [24]. In addition, the optical properties of the antenna are very sensitive to changes in the shape and size of the bowtie nanoantenna [25–27], such as its length, flare angle, feed gap, and thickness. The nonlinear $I(V)$ characteristics of a traveling-wave MIM diode are greatly influenced by the features of the insulating layer, such as its components and geometric parameters [28, 29]. Theoretical simulations have revealed that when a MIM diode is connected to the antenna, the electric field is concentrated in the overlap area of the MIM diode [30, 31], and the electrical signal [32, 33] of the device is at the diode. However, the above calculations consider only the optical and electrical response but give little attention to the optoelectronic properties. Moreover, the obtained optical and electrical signals are not very strong, as the rectenna model needs to be improved. The microscopic mechanism underlying the optoelectronic properties of the rectenna is still unclear because the properties vary with all of the parameters, specifically, the response wavelength, local field enhancement, and output current, which contribute greatly to the design and analysis of the nanoantenna. Therefore, it is extremely important to redesign and optimize the nano-rectenna to obtain better optoelectronic performance as well as better understanding of the microscopic mechanism.

In this work, we proposed and designed an infrared (IR) nano-rectenna composed of a receiving nanoantenna and a MIM diode. The wavelength under study ranges from 5 to 30 μm, as the Earth absorbs solar radiation and reemits it mainly in this wave band, with a peak wavelength of 10.6 μm [32, 34, 35]. The nanoantenna model used in this work is a bowtie nanoantenna because the lightning rod effect can be maximized in this case [18]. The shape of the bowtie is a sector instead of the traditional triangle because a sector antenna can effectively avoid the issue of sharp corners that exists in the traditional triangular antenna, which requires high-precision fabrication. The undesirable singularity issue can thus be eliminated at the extremities in the antenna design by theoretical calculations using HFSS [36]. The MIM diode is a Au–TiO_x–Ti diode because of the large difference in the work function between gold and titanium, which can give rise to a strong rectifying effect. The model construction and calculations are performed entirely by Ansoft HFSS because it can not only calculate the local field enhancement at the center of the antenna gap, but also define many functions such as the output current, induced voltage, and output power owing to the powerful computing capability of the field calculation.

2 Simulations of the nano-rectenna

When IR radiation is incident on a nano-rectenna, the IR AC voltage $V_{IR}\cos(\omega t)$ can be induced at the diode, resulting in a large local field at the tunneling barrier [Fig. 1(a)]. The nonlinear tunneling behavior, which arises from the asymmetry of the diode, leads to a net current flow in one direction and allows the MIM diode to act as a rectifier [14]. To efficiently collect IR radiation, the MIM diode must have a fast response time, which is determined by the speed of electron tunneling. In the equivalent circuit of the nano-rectenna [Fig. 1(b)], the diode consists of a junction capacitor C_D and a nonlinear voltage-dependent resistor $R_D(V)$, which is connected to a resistor R_A in the bowtie nanoantenna. The cutoff frequency is defined as

$$f_c = \frac{1}{2\pi RC_D} = \frac{R_A + R_D(V)}{2\pi R_A R_D(V) C_D}. \tag{1}$$

To minimize the response time of the diode and obtain a high cutoff frequency, the diode capacitance must be small, according to Eq. (1). The diode capacitance C_D is

$$C_D = \frac{\varepsilon_r \varepsilon_0 A}{d}, \tag{2}$$

where ε_r is the relative permittivity of the oxide in the MIM diode, ε_0 is the permittivity of free space, A is the junction area, and d is the oxide thickness. In addition, the dispersion behavior of a metal can be described by the well-known free-electron Drude model [37–39] in order to precisely simulate the variation of the metal permittivity versus the frequency at IR frequencies. The metal's complex relative permittivity function $\varepsilon(\omega)$ can be expressed as

$$\varepsilon(\omega) = \varepsilon_1(\omega) + \mathrm{i}\varepsilon_2(\omega) = 1 - \frac{\omega_p^2}{\omega^2 + \mathrm{i}\omega\gamma_D}, \tag{3}$$

where $\varepsilon_1(\omega)$ and $\varepsilon_2(\omega)$ are the real and imaginary parts, respectively; ω is the angular frequency; $1/\gamma_D$ is the collision frequency; and ω_p is the plasma frequency.

In addition, the dimensions of a nano-rectenna are properly designed to be tens to hundreds of nanometers in the light of successfully fabricated samples [13, 40–42]. The IR rectenna consists of a receiving nanoantenna

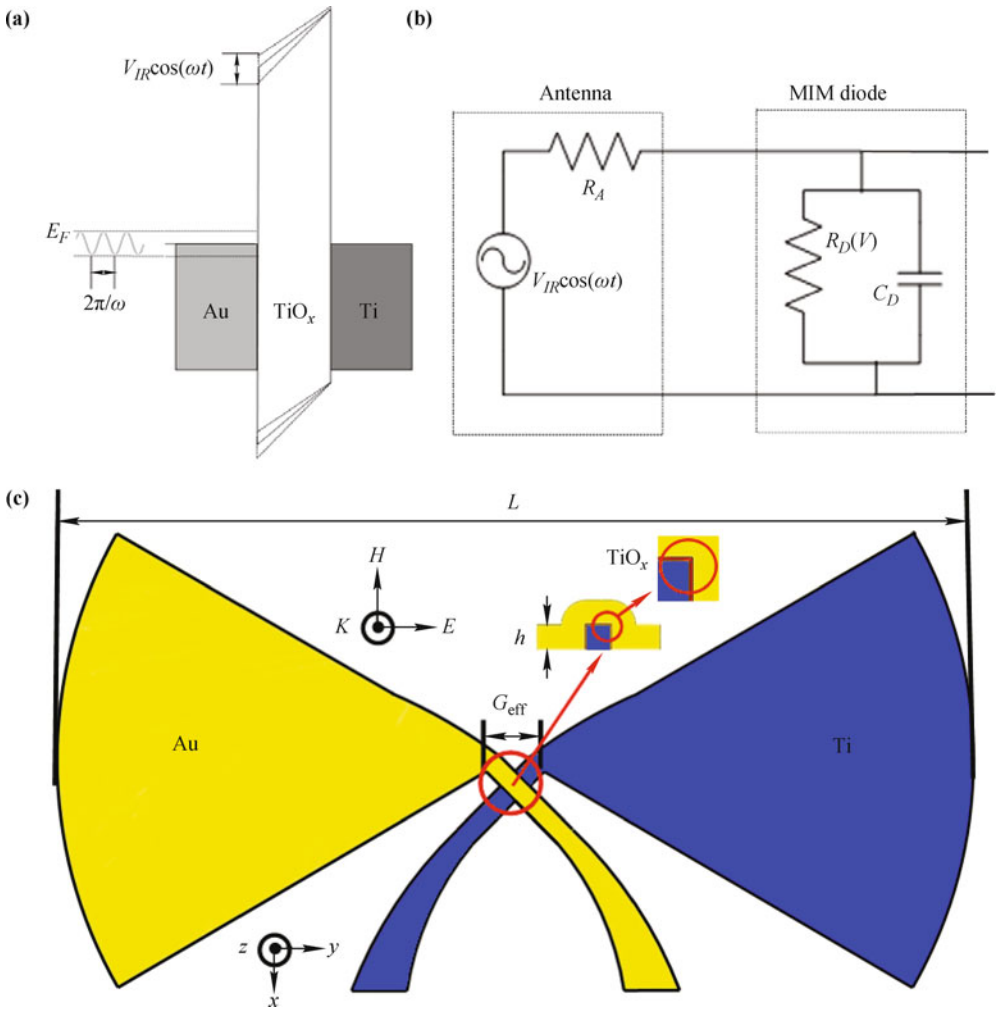

Fig. 1 Design of the sector bowtie nano-rectenna. **(a)** Energy levels of the MIM diode under IR illumination. **(b)** Equivalent circuit of the nano-rectenna. **(c)** The model of the nano-rectenna.

and a THz rectifying diode. The initial length, flare angle, effective gap, and thickness of the antenna are $L = 3.9$ μm, $\theta = 60°$, $G_{eff} = 200$ nm, and $h = 100$ nm, respectively [Fig. 1(c)]. One arm is made of gold, and the other is made of titanium. The TiO_x dielectric layer has a thickness of 5 nm because the MIM resistance increases with increasing oxide thickness [40]. The nano-rectenna is excited by an incident plane wave propagating along the z axis with an electric field intensity of 1 V/m and linear polarization along the antenna axis (y axis). The environment for the simulation is a vacuum.

The electromagnetic wave incident on the bowtie nano-rectenna stimulates surface plasmon oscillations due to the interaction between the incident light and free electrons in the metal, resulting in a huge local field in the dielectric layer of the rectenna. The local field enhancement factor K is defined as $K = |\boldsymbol{E}(\omega)|/|\boldsymbol{E}_0|$, where $\boldsymbol{E}(\omega)$ is the frequency-dependent electric field of the nanoantenna coupled with the incident light. The observation point of the local field enhancement factor K is at the symmetry plane of the nano-rectenna, i.e., the center of the TiO_x dielectric layer. As the frequency changes, the enhancement factor will reach a maximum value K_{max} once surface plasmon resonance occurs, and the resonance wavelength is λ_{rs}. Similarly, on the basis of Maxwell's equations in three-dimensional electromagnetic theory, the output current of a nano-rectenna is described as $\nabla \times \boldsymbol{H} = -\mathrm{i}\omega\varepsilon(\omega)\boldsymbol{E} + \sigma\boldsymbol{E}$, and the induced voltage between the two metal electrodes is expressed as $\nabla \times \boldsymbol{E} = \mathrm{i}\omega\mu\boldsymbol{H}$.

The antenna structure was calculated by the HFSS method and was simulated under radiation boundary condition. In addition, the meshes were further refined until convergence occurred, and the simulations were run long enough to reduce the solution error; i.e., the maximum number of passes was 20, and the maximum delta energy per pass was 0.01. Further, the solution frequency was 28.3 THz, and the sweep frequency ranged from 10

to 60 THz (5–30 μm).

3 Results and discussion

3.1 Antenna length

The calculated resonance spectra of the local field and the output current for different antenna lengths are shown in Fig. 2. Each resonance spectrum has one main resonance peak at wavelengths λ_{rs} of 7.0, 10.0, 12.5, 15.0, and 17.6 μm for antenna lengths L of 2, 3, 4, 5, and 6 μm, respectively. Obviously, a redshift occurs with increasing L. In addition, the intensity of the resonance peak increases monotonically with increasing L. This can be explained using the dipole model [43]. Because a bowtie nanoantenna with symmetrical nanorods is considered a dipole-like antenna, the distance between the positive and negative charges at the ends of both antenna arms increases with increasing L, which weakens the dipole oscillation restoring force. This effect can reduce the oscillation frequency, implying that the resonance wavelength is redshifted. On the other hand, the charges $\boldsymbol{Q}$ accumulated at the ends of both antennas are assumed to remain constant if oscillation occurs according to the equation $\boldsymbol{P} = \boldsymbol{Q} \times \boldsymbol{L}$, where $\boldsymbol{P}$ is the dipole moment. The dipole moment $\boldsymbol{P}$ becomes larger with increasing arm length L; consequently, the resonance intensity increases. As shown in Fig. 2(b), λ_{rs} is almost proportional to L, i.e., $\lambda_{rs} = 2.63 \times L + 1.89$, which is similar to the standing wave model of a dipole antenna, $\lambda_{eff} \times j/2 = L$. Linear relationships are found between the peak intensity and nanoantenna length for both triangular and sector bowtie nanoantennas [Fig. 2(c)], which are expressed as $K_{max} = 83.8 \times L - 114.1$ and $K_{max} = 96.7 \times L - 108.5$, respectively. Thus, the electric field intensity for the triangular antenna is stronger than that for the sector antenna at the same length L. The reason is that the area IR radiation received by the triangular bowtie antenna is slightly larger than that for the sector bowtie antenna; i.e., the number of photons involved in the resonance increases for the former. Moreover, the four sharper corners of the triangle antenna result in a greater free electron density near the corners, so the peak intensity of the triangular antenna is larger than that of the sector antenna. Figure 2(d) shows the output current

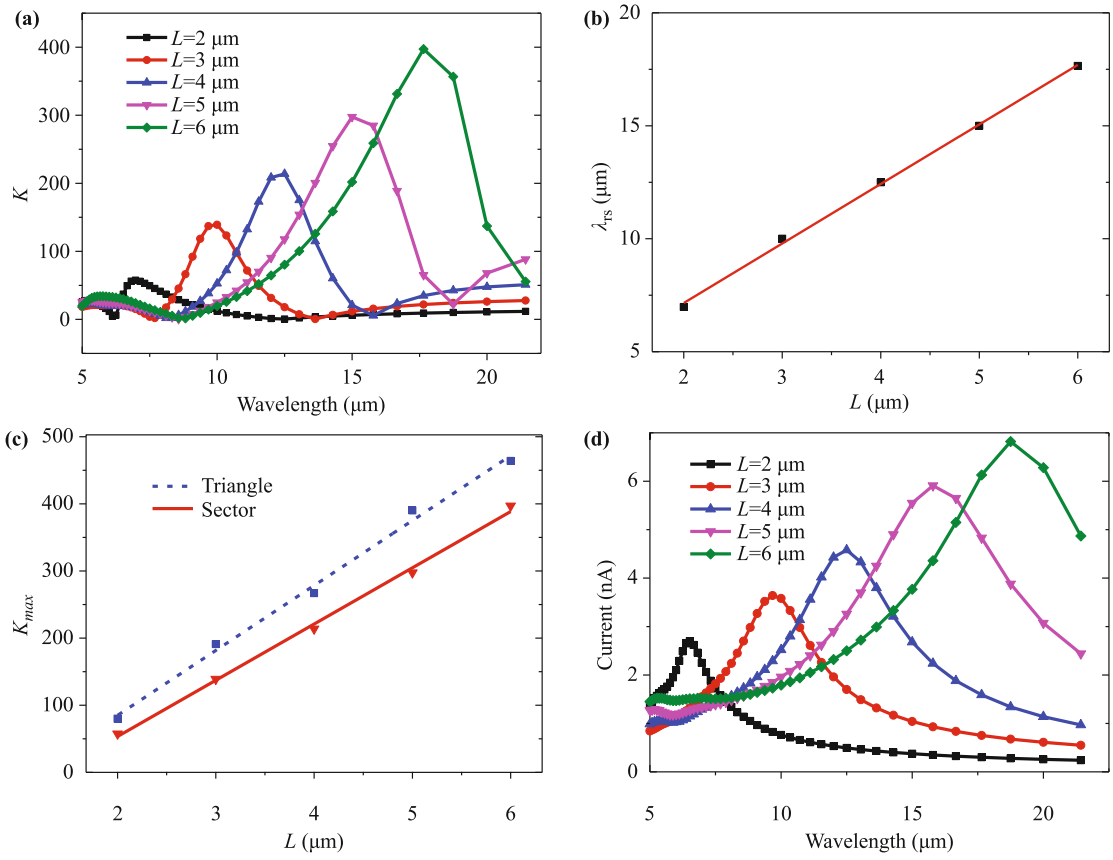

Fig. 2 **(a)** Theoretical calculations of the local field enhancement factor K vs. wavelength at different antenna lengths. **(b)** Resonance wavelength λ_{rs} vs. different antenna lengths. **(c)** Maximum local field enhancement factor K_{max} vs. antenna length of triangle and sector bowtie. **(d)** Output current vs. wavelength at different antenna lengths.

of the antenna with various lengths from the HFSS calculations, where the peak current I_{max} is 2.70, 3.64, 4.58. 5.91, and 6.82 nA for lengths L of 2, 3, 4, 5, and 6 μm, respectively. Thus, the peak current gradually increases with increasing antenna length. This is because of the increasing local field, which results in more photons being absorbed by the dielectric layer, i.e., a higher electromagnetic energy. Therefore, the excited surface plasmon oscillations drive a higher probability for electron tunneling, eventually leading to a higher output current.

3.2 Flare angle

The flare angles of the bowtie nanoantenna reported here are acute because of the geometric requirements when the MIM diode is properly connected to the nanoantenna. The theoretical calculated resonance spectra of the local field, output current, and induced voltage for various flare angles are presented in Fig. 3. The resonance wavelength is 10.3, 11.1, 11.5, 11.8, and 12.0 μm for flare angles θ of 15, 30, 45, 60, and 75°, respectively [Fig. 3(a)]. Thus, the resonance wavelength also exhibits a redshift with increasing flare angle, although its amplitude is not as large as that induced by changes in the antenna length. Moreover, the peak amplitude of the electric field increases with increasing flare angle. The redshift can be explained as [44, 45]

$$\lambda_{rs} \approx 2\int_{-L/2}^{L/2} n_{eff}(x)\mathrm{d}x+\xi, \tag{4}$$

where ξ represents the offset introduced by the interaction of positive and negative charges between the two extremities at the antenna gaps. The variation of ξ with the angle is smaller than the integration term in Eq. (4). Further, λ_{rs} is the resonance wavelength, L is the antenna length, and n_{eff} is the effective index of the local surface plasmon polariton (SPP).

As the flare angle of the bowtie nanoantenna increases, the lateral dimension (i.e., the cross section of the antenna) becomes larger. Consequently, the effective index of the local SPP increases according to the intersection of the dispersion curves of the local SPP [46]. The maximum field enhancement factor K_{max} increases with increasing flare angle, which can be explained by the free electron density at the end of the antenna gap. Increasing the flare angle increases the area of the metal thin film. Thus, the number of free electrons on the antenna surface increases, leading to a larger resonant photon number and free electron density at the feedback of the gap when the other parameters of the antenna are constant. Accordingly, the local electric field is enhanced. Figure 3(b) shows that the peak current and induced voltage increase with increasing flare angle of the antenna. The peak current I_{max} is 3.03, 3.77, 4.24, 4.44, and 4.66 nA for an induced voltage U_{max} of 45.0, 67.3, 104, 106, and 117 nV, respectively. Therefore, the characteristic impedance Z_C of a traveling-wave nano-rectenna is 14.85, 17.85, 22.41, 23.87, and 25.11 Ω, respectively, and exhibits an increasing trend. The surface impedance of the antenna assumed to be the characteristic impedance at high frequencies can be expressed as

$$Z_C = \frac{1}{2\sigma\delta} = \sqrt{\frac{\omega\mu}{8\sigma}}. \tag{5}$$

When the resonance frequency and conductivity are substituted into Eq. (5), the impedance is close to the calculation results shown in Fig. 3(b). As the flare angle increases, in addition, the increasing intensity of the resonance peak gives rise to more oscillating charges on the antenna surface, which exhibits a thermal effect [47]. Hence, the absorption of IR radiation can potentially increase the temperature of the nano-rectenna, decreasing the metallic conductivity and increasing the characteristic impedance.

3.3 Effective gap

Because an optical antenna is usually composed of two sharpened antenna arms facing each other, strong local field enhancement arises in the gap [18]. The coupling strength of the IR radiation to a diode connected to the gap of a nanoantenna is much greater than that to a single diode [13]. Therefore, it is assumed that there is an effective gap G_{eff} between the antenna arms so that the antenna structure can be designed more accurately by theoretical calculation and fabricated more precisely by controlling the experimental conditions. As the effective gap increases from 100 to 400 nm, the resonance wavelength of the antenna shifts very little in the wavelength range of 10–14 μm and is centered at 12 μm [Fig. 4(a)]. The resonance wavelength is centered at 12.5 μm when the effective gap is 500 nm. The results shown in Fig. 4a illustrate that the change in the effective gap between the two arms does not affect the response wavelength in a relatively large range (such as 100–400 nm). In addition, the maximum local field is slightly enhanced with increasing effective gap [Figs. 4(a) and (b)], which may be due to the redistribution of the electric field between the two arms when the diode is connected to the antenna. As the effective gap increases, the positive and negative charges in the two extremities move to the center of the diode, resulting in the enhanced peak electric field. Figure 4(b) shows that the peak current decreases with increasing effective gap. This is because a larger effective

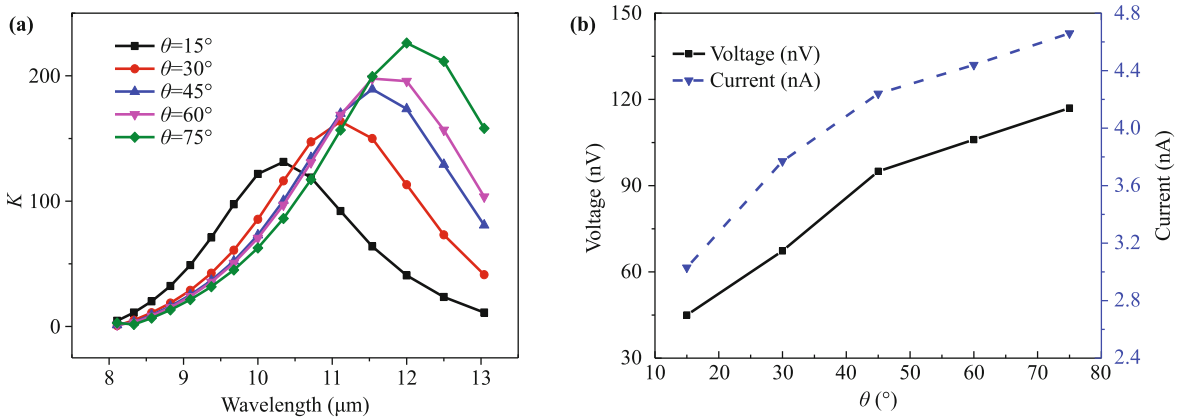

Fig. 3 **(a)** Local field enhancement factor K vs. wavelength at different flare angles. **(b)** Peak current and voltage vs. different flare angles at the resonance wavelengths.

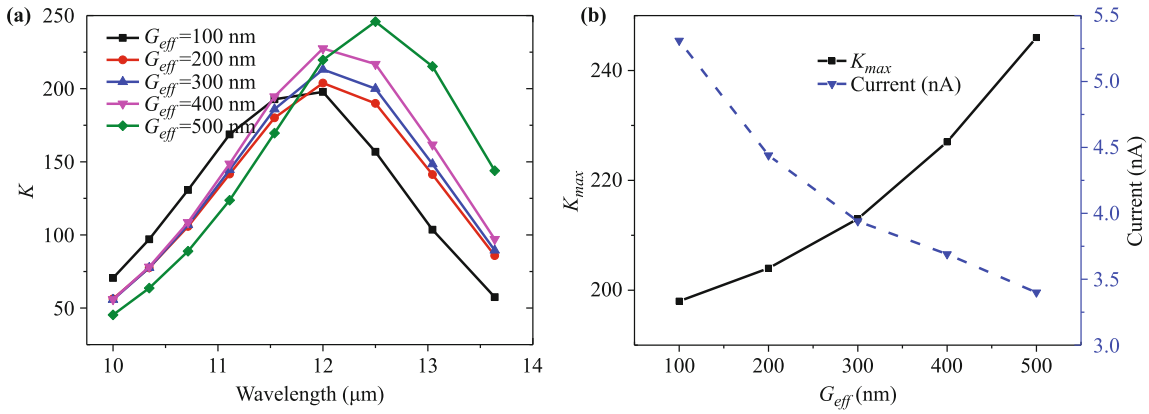

Fig. 4 **(a)** Local field enhancement factor K vs. wavelength at different effective gap. **(b)** Peak field intensity and current vs. different effective gap at the resonance wavelengths.

gap requires longer leads connecting the diode to the antenna, increasing the impedance of the nano-rectenna and possibly causing significant propagation loss of the traveling wave. Thus, the size of the effective gap should be limited to reduce the impedance of the nano-rectenna and the potential propagation loss.

3.4 Antenna thickness

Figure 5 shows the calculated resonance spectra of the local field and the output current for various antenna thicknesses. The resonance wavelength of the antenna, which is centered at 12 μm, shifts very little as the antenna thickness increases from 100 to 200 nm [Fig. 5(a)]. The resonance wavelength is centered at 11.5 μm when the antenna thickness is equal to 50 nm. However, the peak enhancement of the electric field for both the triangular and sector antennas decreases with increasing antenna thickness [Fig. 5(b)], which can be expressed as $K_{max} = -1.21 \times h + 412.3$ and $K_{max} = -0.94 \times h + 316.3$, respectively. This is probably because the air–antenna interface is close to the observation point at small thicknesses. The intensity of the peak field for the triangular bowtie is found to be larger than that for the sector bowtie at the same antenna thickness; the reason may be similar to that for the changes in the antenna length.

Moreover, the output peak current I_{max} is 2.14, 4.14, 5.93, and 7.07 nA for thicknesses h of 50, 100, 150, and 200 nm, respectively [Fig. 5(c)]. Thus, the peak current is enhanced when the antenna thickness increases. This is because a small thickness can increase the antenna impedance. Given that the peak current in Fig. 5c is the total current, the conduction current I_{con} is the real part of the total current, which has the same phase as the electric field. The displacement current I_{dis} is the imaginary part, which is 90° out of phase with the electric field. I_{con} and I_{dis} are 1.37, 2.85, 4.08, and 5.05 nA, and 1.64, 3.00, 4.30, and 4.94 nA [Fig. 5(d)] for thicknesses h of 50, 100, 150, and 200 nm, respectively. Thus, both of them increase with increasing thickness. Because the final rectified DC signal is about half of the output current from the lead after a period, the DC intensity, which can be regarded as the detected DC intensity of the proposed nano-rectenna, is substantially at

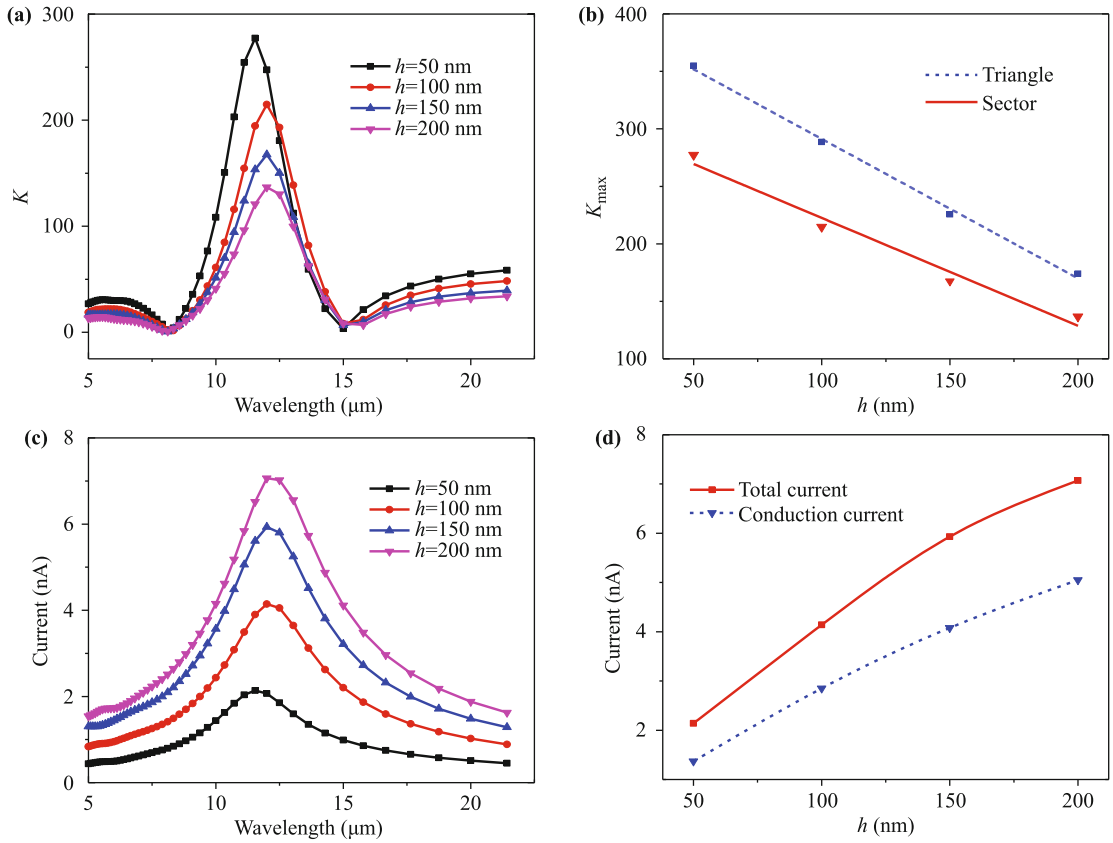

Fig. 5 **(a)** Theoretical calculations of the local field enhancement factor K vs. wavelength at different antenna thicknesses. **(b)** Maximum local field enhancement factor K_{max} vs. antenna thickness for triangle and sector bowtie. **(c)** Output current vs. wavelength at different antenna thicknesses. **(d)** Total current and the conduction current vs. antenna thickness at the resonance wavelengths.

nanoampere magnitude.

3.5 Relative permittivity of TiO_x

For the MIM diode antenna (Au–TiO_x–Ti), the relative permittivity of TiO_x increases when its oxidation degree (x) gradually increases to the stoichiometric TiO_2, (i.e., x changes from 0 to 2), leading to an increasing insulation effect. Because the average dielectric constant of TiO_2 is about 100, the relative permittivity ε_r for TiO_x can be assumed to range from 2 to 100. The calculated resonance spectra of the local field for various relative permittivities of TiO_x are shown in Fig. 6(a). The resonant wavelength (λ_{rs}) is between 11.1 and 12.5 for ε_r values between 2 and 100, indicating that the resonance wavelength is slightly redshifted with increasing relative permittivity of TiO_x. Thus, the response wavelength is not sensitive to the change in the relative permittivity of TiO_x. The minute redshift can be explained by the resonant cavity perturbation theory [26]. For the MIM diode, the electromagnetic field distribution within the cavity is a minor disturbance when the TiO_x dielectric layer is embedded in a metallic cavity composed of gold and titanium. The cavity perturbation can be expressed as

$$\frac{\omega-\omega_0}{\omega} = \frac{-\int\int\int_V [(\Delta\mu\cdot H)\cdot H^* + (\Delta\varepsilon\cdot E)\cdot E^*]\mathrm{d}V}{\int\int\int_V [\mu H\cdot H^* + \varepsilon E\cdot E^*]\mathrm{d}V}, \tag{6}$$

where ω_0 and ω are the pre-perturbation and post-perturbation angular frequencies, respectively. The increase in the permeability ($\Delta\mu$) in the cavity approaches zero. The dielectric constant of TiO_x becomes larger with increasing oxidation degree (i.e., $\Delta\varepsilon > 0$), leading to a slight redshift in the resonance frequency. Further, the peak intensity of the electric field decays exponentially with increasing relative permittivity of TiO_x [Figs. 6(a) and (c)]. This is because the IR radiation coupled by the antenna can excite surface plasmon oscillations in the MIM diode. The evanescent wave generated along the direction of the electric field (i.e., perpendicular to the direction of the antenna surface) decays exponentially with a decay factor of $e^{-\kappa z}$. The decay length is $\kappa^{-1} = \frac{\lambda}{2\pi}\left(\frac{\varepsilon'_m+\varepsilon_d}{\varepsilon_d^2}\right)$, where λ is the wavelength of incident

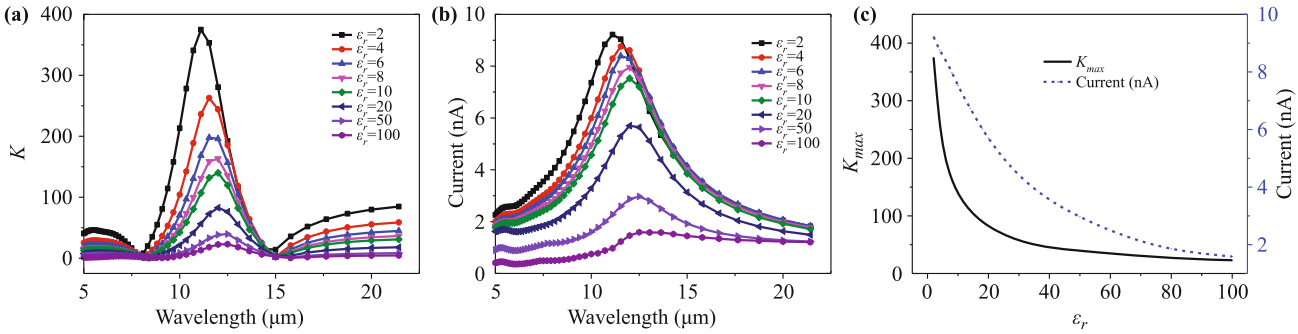

Fig. 6 **(a)** Theoretical calculations of the local field enhancement factor K vs. wavelength at different relative permittivity of TiO_x. **(b)** Output current vs. wavelength at different relative permittivity of TiO_x. **(c)** Peak intensity of electric field and output current vs. relative permittivity of TiO_x at the resonance wavelengths.

light, ε'_m is the real part of the permittivity of the metal, and ε_d is the permittivity of the dielectric material [48]. The peak current falls off rapidly as the relative permittivity of TiO_x increases [Figs. 6(b) and (c)], which is similar to the change in the maximum field intensity. The reason is that the increase in the relative permittivity of TiO_x can increase the height of the barrier formed by the dielectric layer and greatly decrease the probability of electron tunneling, eventually resulting in decreased output current and local field enhancement. In addition, the output current from such a nano-rectenna is proportional to the local electric field and is given by [49, 50]

$$I(\omega) = C(\omega) \oint_S |E|^2 \mathrm{d}S. \tag{7}$$

The proportionality coefficient $C(\omega)$ depends on the properties of the Schottky barrier formed at the interface of the metal and the semiconductor. Eq. (7) shows that the exponential decrease in the local electric field of the diode inevitably causes a substantial decline in the output current, which is consistent with the conclusion above regarding the electron tunneling mechanism.

3.6 Conductivity of TiO_x

In addition to the relative permittivity of TiO_x, the conductivity of the dielectric layer can also affect the rectifying characteristics of the MIM diode nanoantenna. The conductivity of TiO_x gradually increases with decreasing x; namely, TiO_x changes from a semiconductor to a metal. The conductivities of TiO_2, Ti_2O_3, and TiO are about 10^{-8}, 1800, and 3600 S/m, respectively, and that of Ti_2O is assumed to be 10 000 S/m. To simplify the calculation, the conductivity of Ti_nO is set to 100 000 S/m when the value of x is extremely low, i.e., when the characteristics approach those of a metal. The calculated resonance spectra of the local field for TiO_x with various conductivities are shown in Fig. 7(a). The major resonance wavelength λ_{rs} is 13.0, 12.5, 12.5, 12.0, and 11.5 μm for TiO_2, Ti_2O_3, TiO, Ti_2O, and Ti_nO, respectively. The second resonance wavelength exhibits a similar small blueshift with increasing TiO_x conductivity. The fact that the conductivity ($\sigma = ne\mu$) increases in the thin dielectric layer suggests that the carrier concentration n is significantly increased, giving rise to a tremendous increase in the surface charge concentration [51]. This is the main contribution to the formation of high-frequency photons. The high frequency vibration of TiO_x in the dielectric layer results in the blueshift mentioned above [52]. In addition, the intensity of the major peak drops with increasing conductivity, whereas that of the second peak is slightly enhanced. When the conductivity increases to 100 000 S/m, i.e., close to that of the metallic material, the intensity of both peaks becomes very weak, which reveals that the near-field confinement in the dielectric layer weakens, as the reduced insulation reduces the barrier for electron tunneling, and free electrons can thus move directly between the two metals. A high-conductivity dielectric layer such as Ti_nO can cancel the surface plasmon oscillations and electron tunneling mechanism, dramatically decreasing the intensity of the major peak. This can also be explained by the changes in the output current and induced voltage [Fig. 7(b)]. The induced voltage decreases when the dielectric layer changes from TiO_2 to Ti_nO. Further, the amplitude of this reduction increases. The peak current I_{max} is 7.77, 7.26, 6.61, 6.00, and 6.54 nA when the induced voltage U_{max} is 106, 102, 98, 74.1, and 19.1 nV, respectively. However, the output current decreases from TiO_2 to Ti_2O; thus, the increase for Ti_nO is anomalous. This increase results from the decrease in the local field in the dielectric layer with increasing conductivity, which decreases the induced voltage and output current. For the highly conductive Ti_nO, however, the center of the nanoantenna can be regarded as three metal blocks. Thus, there is almost no difference in the transfer of

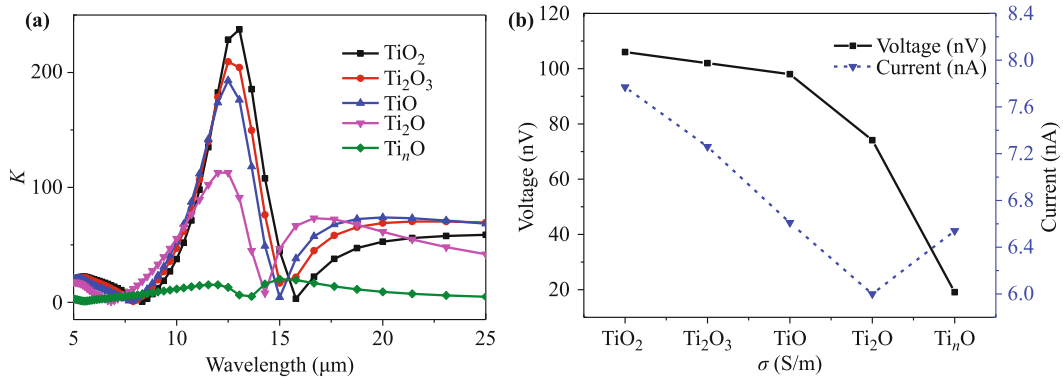

Fig. 7 **(a)** Theoretical calculations of the local field enhancement factor K vs. wavelength at different conductivity of TiO_x. **(b)** Peak current and voltage vs. different ratio of titanium to oxygen at the resonance wavelengths.

electrons under a reverse bias; i.e., an inflection point may exist at some value of n. In this case, the MIM diode structure is possibly destroyed and becomes conductive. Consequently, the rectification mechanism is no longer valid. The significant decrease in the characteristic impedance gives rise to an anomalous increase in the output current.

3.7 Substrate effect and power conversion efficiency

For practical applications, the bowtie nanoantenna is usually fabricated on a dielectric substrate such as glass. In this section, the effect of the substrate on the optical properties of the nano-rectenna is investigated. The preferred antenna structure is designed according to the previous optimization results; the selected length L, flare angle θ, effective gap G_{eff}, thickness h, and relative permittivity ε_r for TiO_x are 4 μm, 60°, 200 nm, 100 nm, and 6, respectively. The effective area of the substrate is designed to be 10 $\mu m\times$ 10 μm, and the thickness is 1 μm. The substrate materials are air (no substrate), silicon dioxide, or silicon, the relative permittivities of which are 1.0006, 4, and 11.9, respectively. The calculated resonance spectra of the local field for these substrates are shown in Fig. 8(a). The resonance wavelengths (λ_{rs}) are 13.0, 17.6, and 25.0 μm when the substrate is air, SiO_2, and Si, respectively. Thus, the resonant wavelength exhibits an obvious redshift as the substrate changes from air to silica to silicon. This redshift can be explained in terms of the wave number, $k = 2\pi n_0/\lambda_0 \approx 2\pi n_1/\lambda_1 \approx 2\pi n_2/\lambda_2$, where n_0, n_1, and n_2 are the refractive indices of air, SiO_2, and Si, respectively, and λ_0, λ_1, and λ_2 are the corresponding resonance wavelengths. When the IR radiation coupled by the bowtie nanoantenna propagates at the interface of the antenna and the substrate, the wave number adjacent to the substrate is approximately the same owing to the boundary conditions of the electromagnetic field. In other words, the redshift occurs because the refractive index of the substrate increases as $n_0 < n_1 < n_2$. In addition, the maximum local field enhancement factor K_{max} is found to be 237.4, 342.3, and 763.7 V/m for the air, SiO_2, and Si substrates, respectively. Thus, K_{max} increases with increasing relative permittivity of the substrate. As shown in Fig. 8(b), the field distribution of the substrates in the $z = 0$ plane is concentrated in a very thin insulating layer, where the electric field decreases gradually toward the outermost edge of the insulating layer and has an approximately symmetrical distribution on both sides. When the substrate changes from the air to silica and then to pure silicon, the local field intensity increases, which is consistent with the results shown in Fig. 8(a). This can be explained by the decay length of surface plasmons, i.e., $\kappa^{-1} = \frac{\lambda}{2\pi}\left(\frac{\varepsilon'_m+\varepsilon_d}{\varepsilon_d^2}\right)$. The decay length decreases when the relative permittivity of the substrate increases, resulting in more localization in the z direction and therefore a stronger local field.

For the bowtie nanoantenna, the power conversion efficiency can be defined as $f = P_{out}/P_{in}$, where P_{in} is the input power of the nano-rectenna, and P_{out} is its output power (i.e., the received power in the tunnel junction). The input power $P_{in} = I_0 \cdot A$, where A is the area that receives the radiation in a bowtie nanoantenna, and I_0 is the incident light intensity. $I_0 = \frac{1}{2}\sqrt{\frac{\varepsilon}{\mu}} \cdot E \cdot E^* = \frac{1}{2\eta} E_0^2$, where η is the wave impedance in a medium. When the environment is under vacuum, η equals 377 Ω. The output power $P_{out} = \frac{1}{2} Re(\oint_S \boldsymbol{S} \mathrm{d}S)$, where $\boldsymbol{S}$ is the Poynting vector ($\boldsymbol{S} = \boldsymbol{E} \times \boldsymbol{H}$). The maximum output power P_{max} is 1.89×10^{-16}, 2.78×10^{-16}, and 6.16×10^{-16} W for the air, SiO_2, and Si substrates, respectively [Fig. 8(c)]. Thus, P_{max} shows an increasing trend when the substrate changes from air to silica and then to pure silicon. The incident light intensity is 1.33×10^{-3} W/m^2 when the electric field intensity is 1 V/m. The area A ($\approx 0.25\theta L^2$) is 4.19×10^{-12} m^2 when the antenna length

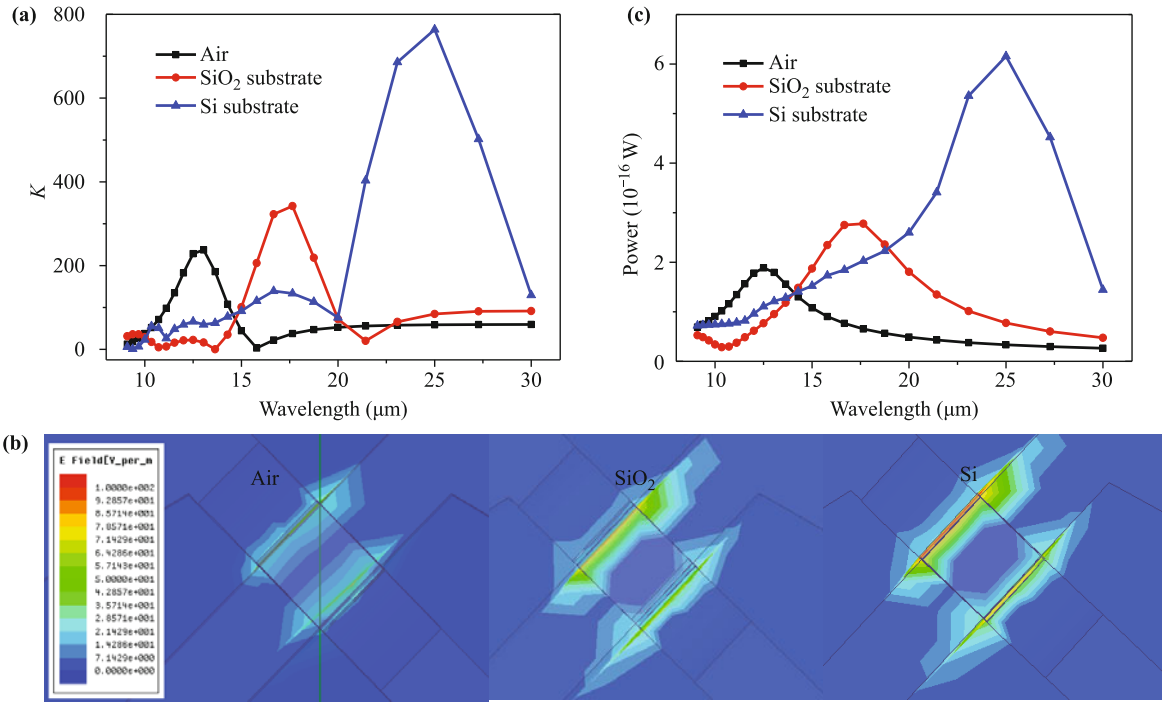

Fig. 8 **(a)** Theoretical calculations of the local field enhancement factor K vs. wavelength at different substrates. **(b)** Electric field distribution in the $z = 0$ plane for different substrates. **(c)** Output power of the antenna diode vs. wavelength for different substrate.

L is 4 μm. The input power (P_{in}) is 5.57×10^{-15} W. Thus, the power conversion efficiency for the three substrates at the resonant wavelength is determined to be 3.4% [f(air)], 5.0% [$f(SiO_2)$], and 11.1% [f(Si)]. For practical applications, accordingly, various conversion efficiencies can be achieved by choosing different substrates to fabricate the device according to the response wavelength.

4 Conclusions

In summary, we systematically studied a sector bowtie nano-rectenna coupling mid- and far-IR radiation using the Ansoft HFSS method. The theoretical results indicate that many factors can significantly affect the optical and electrical properties of the nano-rectenna. The resonance wavelength is redshifted when the antenna length, flare angle, and relative permittivity of TiO_x increase, whereas it is slightly blueshifted when the conductivity of TiO_x increases. The maximum intensity of the local field increases when the antenna length, flare angle, and effective gap increase, whereas it decreases with increasing antenna thickness, relative permittivity, and conductivity of TiO_x. The output current rectified by the MIM diode is substantially at nanoampere magnitude when the incident electric field intensity is 1 V/m, and the induced voltage of the rectenna is about 100 nV. When the optimized nano-rectenna is fabricated using different substrates (air, SiO_2, and Si), the resonance wavelength is redshifted and the maximum field intensity increases with increasing refractive index of the substrate; the power conversion efficiency also increases from 3.4% to 5.0% and then to 11.1%. These results may provide good theoretical support for the design and fabrication of nano-rectenna devices that can efficiently use IR energy by modulating various parameters, especially by considering the following three points.

(i) The antenna length and refractive index of the substrate are the major parameters affecting the response frequency, as the other parameters do not significantly affect the peak shift. For instance, the length of the antenna with a low-refractive-index substrate should be controlled at around 3–4 μm to obtain a response near 10.6 μm, whereas the length of the antenna should be shortened appropriately when a substrate with a high refractive index is used.

(ii) For the local field intensity, the antenna length, antenna thickness, and relative permittivity of the dielectric layer strongly affect the IR radiation coupled by the nanoantenna. To obtain strong local field enhancement, therefore, the antenna length and the refractive index of the substrate should be increased appropriately, whereas the antenna thickness and the relative permittivity of the dielectric layer should be reduced accordingly.

(iii) Regarding the electrical properties of the nano-rectenna, the output current is greatly affected by all

of the parameters except for the flare angle. To increase the final output signal, the length of the antenna should be suitably increased. In addition, the effective gap and the relative permittivity and conductivity of the dielectric layer should be decreased. A dielectric layer with a certain level of insulation favors impedance matching between the antenna and the diode, resulting in an increased rectifying effect.

Acknowledgements This work was supported by the Ministry of Science and Technology of China (Grant No. 2015DFG62610) and the National Natural Science Foundation of China (Grant No. 11404074).

References

1. K. Shankar, J. Bandara, M. Paulose, H. Wietasch, O. K. Varghese, G. K. Mor, T. J. LaTempa, M. Thelakkat, and C. A. Grimes, Highly efficient solar cells using TiO_2 nanotube arrays sensitized with a donor-antenna dye, *Nano Lett.* 8(6), 1654 (2008)
2. G. Gol'Tsman, O. Okunev, G. Chulkova, A. Lipatov, A. Semenov, K. Smirnov, et al., Picosecond superconducting single-photon optical detector, *Appl. Phys. Lett.* 91, 012002 (2003)
3. R. Gordon, D. Sinton, K. L. Kavanagh, and A. G. Brolo, A new generation of sensors based on extraordinary optical transmission, *Acc. Chem. Res.* 41(8), 1049 (2008)
4. I. Friedler, C. Sauvan, J. P. Hugonin, P. Lalanne, J. Claudon, and J. M. Gérard, Solid-state single photon sources: the nanowire antenna, *Opt. Express* 17(4), 2095 (2009)
5. A. Langari and H. Hashemi, A cooling solution for power amplifier modules in cellular phone applications, *Electronic Components and Technology Conference 49th.* 316–320 (1999)
6. C. R. Williams, S. R. Andrews, S. Maier, A. Fernández-Domínguez, L. Martín-Moreno, and F. García-Vidal, Highly confined guiding of terahertz surface plasmon polaritons on structured metal surfaces, *Nat. Photonics* 2(3), 175 (2008)
7. P. Neutens, L. Lagae, G. Borghs, and P. Van Dorpe, Electrical excitation of confined surface plasmon polaritons in metallic slot waveguides, *Nano Lett.* 10(4), 1429 (2010)
8. K. A. Willets, Plasmon point spread functions: How do we model plasmon-mediated emission processes? *Front. Phys.* 9(1), 3 (2014)
9. Y. L. Zhao, Y. L. Song, W. G. Song, W. Liang, X. Y. Jiang, Z. Y. Tang, H. X. Xu, Z. X. Wei, Y. Q. Liu, M. H. Liu, L. Jiang, X. H. Bao, L. J. Wan, and C. L. Bai, Progress of nanoscience in China, *Front. Phys.* 9(3), 257 (2014)
10. A. Ono, M. Kikawada, W. Inami, and Y. Kawata, Surface plasmon coupled fluorescence in deep-ultraviolet excitation by Kretschmann configuration, *Front. Phys.* 9(1), 60 (2014)
11. D. K. Gramotnev and S. I. Bozhevolnyi, Plasmonics beyond the diffraction limit, *Nat. Photonics* 4(2), 83 (2010)
12. R. F. Oulton, V. J. Sorger, T. Zentgraf, R. M. Ma, C. Gladden, L. Dai, G. Bartal, and X. Zhang, Plasmon lasers at deep subwavelength scale, *Nature* 461(7264), 629 (2009)
13. C. Fumeaux, W. Herrmann, F. Kneubühl, and H. Rothuizen, Nanometer thin-film Ni–NiO–Ni diodes for detection and mixing of 30 THz radiation, *Infrared Phys. Technol.* 39(3), 123 (1998)
14. J. A. Bean, A. Weeks, and G. D. Boreman, Performance optimization of antenna-coupled tunnel diode infrared detectors, *Quantum Electron.* 47(1), 126 (2011)
15. Z. Zhu, S. Joshi, and G. Moddel, High performance room temperature rectenna IR detectors using graphene geometric diodes, *Selected Topics in Quantum Electronics* 20, (2014)
16. L. Son, T. Tachiki, and T. Uchida, Fabrication of VOx microbolometer detector coupled with thin-film spiral antenna by metal-organic decomposition, *37th International Conference on Infrared, Millimeter, and Terahertz Waves (IRMMW-THz)* 1–2 (2012)
17. S. Krishnan, H. La Rosa, E. Stefanakos, S. Bhansali, and K. Buckle, Design and development of batch fabricatable metal–insulator–metal diode and microstrip slot antenna as rectenna elements, *Sens. Actuators A Phys.* 142(1), 40 (2008)
18. K. Choi, F. Yesilkoy, G. Ryu, S. H. Cho, N. Goldsman, M. Dagenais, and M. Peckerar, A focused asymmetric metal–insulator–metal tunneling diode: Fabrication, DC characteristics and RF rectification analysis, *IEEE Trans. Electron. Dev.* 58(10), 3519 (2011)
19. S. Zhang, L. Wang, C. Xu, D. Li, L. Chen, and D. Yang, Fabrication of Ni-NiO-Cu metal-insulator-metal tunnel diodes via anodic aluminum oxide templates, *ECS Solid State Letters* 2(1), Q1 (2012)
20. M. Gadalla, M. Abdel-Rahman, and A. Shamim, Design, Optimization and Fabrication of a 28.3 THz Nano-Rectenna for Infrared Detection and Rectification, *Scientific reports* 4, (2014)
21. P. Mühlschlegel, H. J. Eisler, O. Martin, B. Hecht, and D. Pohl, Resonant optical antennas, *Science* 308(5728), 1607 (2005)
22. D. P. Fromm, A. Sundaramurthy, P. J. Schuck, G. Kino, and W. Moerner, Gap-dependent optical coupling of single "bowtie"nanoantennas resonant in the visible, *Nano Lett.* 4(5), 957 (2004)
23. A. Sundaramurthy, K. Crozier, G. Kino, D. Fromm, P. Schuck, and W. Moerner, Field enhancement and gapdependent resonance in a system of two opposing tip-to-tip Au nanotriangles, *Phys. Rev. B* 72(16), 165409 (2005)
24. F. J. González, J. Alda, J. Simón, J. Ginn, and G. Boreman, The effect of metal dispersion on the resonance of antennas at infrared frequencies, *Infrared Phys. Technol.* 52(1), 48 (2009)
25. A. Alù and N. Engheta, Input impedance, nanocircuit loading, and radiation tuning of optical nanoantennas, *Phys. Rev. Lett.* 101(4), 043901 (2008)
26. T. R. Lin, S. W. Chang, S. L. Chuang, Z. Zhang, and P. J. Schuck, Coating effect on optical resonance of plasmonic

nanobowtie antenna, *Appl. Phys. Lett.* 97(6), 063106 (2010)

27. S. Choi, and K. Sarabandi, Design optimization of bowtie nanoantenna for high-efficiency thermophotovoltaics, *2013 US National Committee of URSI National in Radio Science Meeting (USNC-URSI NRSM)* 1–1 (2013)
28. J. W. Liaw, Analysis of a bowtie nanoantenna for the enhancement of spontaneous emission, *IEEE J. Sel. Top. Quantum Electron.* 14(6), 1441 (2008)
29. X. Lei, and V. Van, FDTD modeling of traveling-wave MIM diode for ultrafast pulse detection, *Opt. Commun.* 294, 344 (2013)
30. A. Sabaawi, C. Tsimenidis, and B. Sharif, Bow-tie nanoarray rectenna: Design and optimization, *2012 6th Euro-pean Conference in Antennas and Propagation (EUCAP)* 1975-1978 (2012)
31. L. P. Xia, Z. Yang, S. Y. Yin, W. R. Guo, J. L. Du, and C. L. Du, Hole arrayed metalinsulator-metal structure for surface enhanced Raman scattering by self-assembling polystyrene spheres, *Front. Phys.* 9(1), 64 (2014)
32. A. M. Sabaawi, C. C. Tsimenidis, and B. S. Sharif, Analysis and modeling of infrared solar rectennas, *IEEE J. Sel. Top. Quantum Electron.* 19(3), 9000208 (2013)
33. E. Briones, J. Alda, and F. J. González, Conversion efficiency of broad-band rectennas for solar energy harvesting applications, *Opt. Express* 21(S3), A412 (2013)
34. D. K. Kotter, S. D. Novack, W. Slafer, and P. Pinhero, Theory and manufacturing processes of solar nanoantenna electromagnetic collectors, *J. Sol. Energy Eng.* 132(1), 011014 (2010)
35. M. Gallo, L. Mescia, O. Losito, M. Bozzetti, and F. Prudenzano, Design of optical antenna for solar energy collection, *Energy* 39(1), 27 (2012)
36. Y. M. Wu, L. W. Li, and B. Liu, Gold bow-tie shaped aperture nanoantenna: Wide band near-field resonance and farfield radiation, *IEEE Trans. Magn.* 46(6), 1918 (2010)
37. M. A. Ordal, R. J. Bell, R. W. Jr Alexander, L. L. Long, and M. R. Querry, Optical properties of fourteen metals in the infrared and far infrared: Al, Co, Cu, Au, Fe, Pb, Mo, Ni, Pd, Pt, Ag, Ti, V, and W, *Appl. Opt.* 24(24), 4493 (1985)
38. T. Schumacher, K. Kratzer, D. Molnar, M. Hentschel, H. Giessen, and M. Lippitz, Nanoantenna-enhanced ultrafast nonlinear spectroscopy of a single gold nanoparticle, *Nat. Commun.* 2, 333 (2011)
39. M. Husnik, S. Linden, R. Diehl, J. Niegemann, K. Busch, and M. Wegener, Quantitative experimental determination of scattering and absorption cross-section spectra of individual optical metallic nanoantennas, *Phys. Rev. Lett.* 109(23), 233902 (2012)
40. I. Wilke, Y. Oppliger, W. Herrmann, and F. Kneubühl, Nanometer thin-film Ni-NiO-Ni diodes for 30 THz radiation, *Appl. Phys. A* 58(4), 329 (1994)
41. C. Fumeaux, W. Herrmann, H. Rothuizen, P. De Natale, and F. Kneubühl, Mixing of 30 THz laser radiation with nanometer thin-film Ni-NiO-Ni diodes and integrated bowtie antennas, *Appl. Phys. B* 63(2), 135 (1996)
42. C. Fumeaux, G. D. Boreman, W. Herrmann, F. K. Kneubühl, and H. Rothuizen, Spatial impulse response of lithographic infrared antennas, *Appl. Opt.* 38(1), 37 (1999)
43. J. Aizpurua, G. W. Bryant, L. J. Richter, F. J. García de Abajo, B. K. Kelley, and T. Mallouk, Optical properties of coupled metallic nanorods for field-enhanced spectroscopy, *Phys. Rev. B* 71(23), 235420 (2005)
44. W. Ding, R. Bachelot, S. Kostcheev, P. Royer, and R. E. de Lamaestre, Surface plasmon resonances in silver Bowtie nanoantennas with varied bow angles, *J. Appl. Phys.* 108(12), 124314 (2010)
45. L. Novotny, Effective wavelength scaling for optical antennas, *Phys. Rev. Lett.* 98(26), 266802 (2007)
46. W. Ding, S. Andrews, and S. Maier, Internal excitation and superfocusing of surface plasmon polaritons on a silvercoated optical fiber tip, *Phys. Rev. A* 75(6), 063822 (2007)
47. Z. J. Coppens, W. Li, D. G. Walker, and J. G. Valentine, Probing and controlling photothermal heat generation in plasmonic nanostructures, *Nano Lett.* 13(3), 1023 (2013)
48. W. L. Barnes, A. Dereux, and T. W. Ebbesen, Surface plasmon subwavelength optics, *Nature* 424(6950), 824 (2003)
49. A. Novitsky, A. Uskov, C. Gritti, and I. Protsenko, Photon absorption and photocurrent in solar cells below semiconductor bandgap due to electron photoemission from plasmonic nanoantennas, *Prog. Photovolt. Res. Appl.* (2012)
50. S. V. Zhukovsky, V. E. Babicheva, A. V. Uskov, I. E. Protsenko, and A. V. Lavrinenko, Enhanced electron photoemission by collective lattice resonances in plasmonic nanoparticle-array photodetectors and solar cells, *Plasmonics* 9(2), 283 (2014)
51. P. C. Chang, C. J. Chien, D. Stichtenoth, C. Ronning, and J. G. Lu, Finite size effect in ZnO nanowires, *Appl. Phys. Lett.* 90(11), 113101 (2007)
52. J. Li, C. Wang, H. Peng, M. Wang, R. Zhang, H. Wang, J. Liu, M. L. Zhao, and L. M. Mei, Vibrational and thermal properties of small diameter silicon nanowires, *J. Appl. Phys.* 108(6), 063702 (2010)